npj | biofilms and microbiomes

Article

Published in partnership with Nanyang Technological University

https://doi.org/10.1038/s41522-025-00670-5

Population-level control of two manganese oxidases expands the niche for bacterial manganese biomineralization

Gaitan Gehin[1], Nicolas Carraro[2], Jan Roelof van der Meer[2] & Jasquelin Peña[1,3] ✉

The enzymatic oxidation of aqueous divalent manganese (Mn) is a widespread microbial trait that produces reactive Mn(III, IV) oxide minerals. These biominerals drive carbon, nutrient, and trace metal cycles, thus playing important environmental and ecological roles. However, the regulatory mechanisms and physiological functions of Mn biomineralization are unknown. This challenge arises from the common occurrence of multiple Mn oxidases within the same organism and the use of Mn oxides as indicators of combined gene activity. Through the detection of gene activation in individual cells, we discover that expression of *mnxG* and *mcoA*, two Mn oxidase-encoding genes in *Pseudomonas putida* GB-1, is confined to subsets of cells within the population, with each gene showing distinct spatiotemporal patterns that reflect local microenvironments. These coordinated intra-population dynamics control Mn biomineralization and illuminate the strategies used by microbial communities to dictate the extent, location, and timing of biogeochemical transformations.

Life and minerals are inextricably linked[1–8]. In microorganisms, biomineralization—the process of mineral precipitation through biological activity—serves many physical, chemical, and biological functions[2]. These functions include protection from UV radiation, antibiotics, or encrustation; detoxification of reactive oxygen species, CO_2, or other toxic compounds; and storage of nutrients, carbon, or energy. Biomineralization also supports microbial metabolism by allowing some microorganisms to generate additional proton motive force, conduct extracellular electron transfer, or colonize environmental niches at redox interfaces[2,9–13]. For some systems such as manganese (Mn)[14], however, the mechanisms and functions of biomineralization are partially or scarcely known.

Mn biomineralization is a widespread microbial trait performed by a phylogenetically diverse group of bacteria and fungi[15–18]. Mn-oxidizing microorganisms are found in numerous aquatic and terrestrial environments[5,19,20]. They typically use one or more multicopper oxidase (MCO) or animal heme peroxidase enzymes[15,18] to oxidize aqueous Mn(II) to Mn(III, IV) species, which subsequently precipitate as reactive layer-type Mn oxides[5,20]. A recent genome meta-analysis showed the wide conservation of multicopper Mn-oxidase genes in 682 out of 2197 tested bacterial genomes, and found co-occurring MCOs in a third of the predicted Mn oxidizers[15]. The enzymatic reaction involves extracellular or membrane-bound enzymes and electron transfer chains that donate up to two electrons from Mn(II) species to molecular oxygen and, in some cases, H_2O_2[17]. The rates of enzymatic Mn(II) oxidation are up to five orders of magnitude faster than expected from homogeneous aqueous-phase reactions or heterogeneous reactions between aqueous and solid-phase species[21], suggesting that this process has one or more critical biological functions. However, how and under which extracellular environmental conditions the expression of Mn oxidases is regulated by the cell, how this contributes to mineral precipitation, and whether this process benefits microbial life remains largely unknown.

A key challenge in advancing our understanding of the functional role(s) of bacterial Mn biomineralization is that this complex process cannot be measured or described by any single endpoint. Mn-oxidizing enzymes have been purified or partially purified, and their catalytic activity has been studied, notably with model Mn oxidizers such as *Bacillus sp.* PL-12[14,22,23], *Roseobacter* AzwK-3b[24,25], and especially *Pseudomonas putida* GB-1[15,26–32]. Nonetheless, to address the functional and ecological roles of Mn oxidation and biomineralization, the enzymes need to be studied at the individual cell and population level. To date, most studies of enzymatic manganese oxidation and biomineralization rely on the quantification of the Mn oxide itself, which is problematic for a number of reasons. Biogenic Mn oxides form extracellularly[17,22,26,29,33] and often in a matrix of extracellular polymeric substances, which results in complex microbe-mineral assemblages[34]. Manganese oxides are also highly reactive towards metals[35,36] and are susceptible to reductive dissolution in the presence of organic compounds and extracellular metabolites such as sugars, organic acids, and siderophores[17,37–39]. Therefore, using redox-sensitive Mn oxides as indicators

[1]Department of Civil and Environmental Engineering, University of California, Davis, CA, USA. [2]Department of Fundamental Microbiology, University of Lausanne, Vaud, CH, Switzerland. [3]Energy Geosciences Division, Lawrence Berkeley National Laboratory, Berkeley, CA, USA. ✉e-mail: pena@ucdavis.edu

of Mn oxidase gene expression and enzymatic activity can lead to an incomplete understanding of the mechanisms of Mn oxidation. This approach is further obfuscated by the presence of multiple Mn oxidases and multiple regulation pathways within the same organism[15,24,27,40,41]. To overcome these challenges, two key advances are required: the enzymatic activity must be decoupled from Mn oxide formation, and Mn-oxidase gene activation must be linked to mineral precipitation at the level of individual cells within bacterial populations.

Our goal here was thus to develop a system to disentangle the dynamics of Mn-oxidase gene activation alongside Mn oxide formation as a function of environmental growth conditions. As a model system, we used *Pseudomonas putida* GB-1, a bacterium that has been shown to possess three genes for Mn oxidation: two multicopper oxidases (MnxG and McoA) and a heme peroxidase (MopA)[28]. Both MnxG and McoA can catalyze Mn oxidation independently, as shown in a study of *P. putida* GB-1 derivatives with in-frame deletions of either *mnxG* or *mcoA*[26]. To follow Mn-oxidase gene activation at the single-cell level, we constructed reporter gene fusions in wild-type *P. putida* GB-1, a strain containing all the genetic material required for Mn oxidation. These fusions consist of a single, chromosomally-integrated copy of the promoter regions upstream of either *mnxG* or *mcoA* (designated as *P2447_mnxG* and *P2665_mcoA*, respectively, and hereafter as P_{mnxG} and P_{mcoA}. While each fusion strain reports only one gene, the organisms contain the full genetic background for manganese oxidation. We did not select *mopA* as a reporter gene because it has never shown any activity in the wild-type strain or mutants lacking both *mnxG* and *mcoA*[42]. We anticipated that cells activating either promoter would trigger the formation of the reporter fluorescence, which serves as a proxy for Mn-oxidase expression. Fluorescent reporters also provide signals that can be quantified using microscopy in real-time in individual cells, allowing us to detect Mn-oxidase activation over time as a function of spatial position. To create different physiological conditions, we cultured GB-1 on surfaces and in liquid suspension to follow Mn-oxidase gene expression in microcolonies as well as in individual planktonic cells and cell aggregates (*P. putida* GB-1 quickly forms strongly adhering multi-cell aggregates[34]), respectively.

We show that *mnxG* and *mcoA* are successively activated in non-dividing cells in the stationary phase, only in the presence of Mn, and independently of the growth condition. By simultaneously localizing Mn oxide formation to reporter expression, we find that MnxG is responsible for the initial precipitation of Mn oxides, and McoA contributes to biomineralization under conditions where MnxG activity is restricted. Mn-oxidase gene activation and mineral precipitation occurred only in a subpopulation of cells, whose proportion is not dependent on planktonic or sessile lifestyle, but rather is determined by local environmental conditions. The discovery of subpopulation-dependent Mn-oxidase expression in GB-1 provides a new framework for understanding the cellular function(s) of Mn oxidation and biomineralization, which we hypothesize may involve cellular cooperation to dictate the need, location, and timing of the Mn transformation reactions.

Results

Decoupling gene activation from Mn oxide precipitation

To facilitate the detection of Mn oxidase gene expression in *P. putida* GB-1, we constructed two derivative strains with eCherry fused to the isolated promoters of either *mnxG* or *mcoA* (Supplementary Figs. 1 and 2). Reporter fusions were placed in a single gene copy on the *P. putida* GB-1 chromosome and shielded for upstream and downstream transcription read-through. These derivative strains contain the complete Mn-oxidizing machinery and report either *mnxG* or *mcoA* activation (hereafter, bioreporters). Sequence analysis revealed a similar structure for the two promoter regions upstream of *mnxG* (P_{mnxG}) and *mcoA* (P_{mcoA}), with each containing the predicted binding sites for integration host factor (IHF) and sigma-54 (σ^{54}) transcription factor (Supplementary Fig. 1). The binding site suggested that both genes are IHF-σ^{54} dependent promoters, whose activation is frequently associated to stationary phase conditions[43,44] and regulated by specific environmental signals[45–48]. Reporter gene activation in both strains then serves as a proxy for Mn-oxidase gene expression that can be compared to the precipitation of Mn oxides, allowing us to quantify biological and geochemical expressions of Mn biomineralization.

Mn triggers the activation of P_{mnxG} and P_{mcoA} promoters

To examine the activation of *mnxG* and *mcoA* promoters, we recorded eCherry fluorescence signals in cells of wild-type *P. putida* GB-1, the P_{mnxG} bioreporter, and the P_{mcoA} bioreporter after 48 h in the presence or absence of 50 μM $MnCl_2$. Experiments were carried out using cells grown on solid agarose surfaces (Fig. 1) or in liquid-suspended culture (Supplementary Fig. 3). In the absence of Mn, there was no difference between the fluorescence intensity of the bioreporters and the wild-type auto-fluorescence in the eCherry wavelengths (Fig. 1a, b). In the presence of 50 μM $MnCl_2$, the median bioreporter signal for P_{mnxG} in surface-grown microcolonies increased by 12.5-fold, and that of P_{mcoA} increased by 4.7-fold relative to the no Mn condition (Fig. 1a, b). In liquid-suspended culture, the median fluorescence signal of the P_{mnxG} bioreporter in the presence of 50 μM $MnCl_2$ increased by 16-fold and that of P_{mcoA} by 13-fold, compared to the no Mn condition (Supplementary Fig. 3). These results show that Mn is required for the activation of the *mnxG* and *mcoA* promoters.

Stationary phase and subpopulation-dependent activation of P_{mnxG} and P_{mcoA}

The bioreporter signals of individual cells within microcolonies grown in the presence of Mn, measured after 48 h, differed widely (Fig. 1c, d). Specifically, the distribution of pixel intensities in 21 microcolonies of the P_{mnxG} bioreporter showed three distinct modes: one below the fluorescence threshold and two above the fluorescence threshold. This pattern in the fluorescence signal distribution within the microcolonies suggests bimodal gene activation, where P_{mnxG} is inactive in one subpopulation of cells and active in another. The occurrence of two modes at 1600 a.u. and 2500 a.u. may result from the increased stacking of cells near the microcolony centre relative to the microcolony edges. The pixel intensities of the P_{mcoA} bioreporter in 45 microcolonies grown in the presence of Mn showed two modes, one at 60 a.u. and another at 2240 a.u. The higher proportion of fluorescence intensities below the threshold than above the threshold suggests that the P_{mcoA} promoter was inactive in most of the population and less transcribed overall than the P_{mnxG} promoter (Fig. 1a, b).

To confirm the bimodality of the gene activation pattern for P_{mnxG} and P_{mcoA}, we monitored bioreporter activation over time in growing microcolonies. The maximum exponential growth rates (μ), calculated as the increase in projected surface area over time, were comparable for both bioreporters, with an average of $\mu = 0.19 \pm 0.02\ h^{-1}$ for strain P_{mnxG} and $\mu = 0.13 \pm 0.07\ h^{-1}$ for strain P_{mcoA}, and entry into stationary phase at 19.5 h and 19.0 h, respectively, for strain P_{mnxG} and strain P_{mcoA} (Fig. 2a, b). The timing of microcolony growth compared to the appearance of the reporter signals indicated that both promoters were activated exclusively after entry into stationary phase (Fig. 2a, b), as confirmed further by the disappearance of the fluorescence reporter signal in stationary phase cells exposed to fresh growth medium (Supplementary Fig. 4). However, the fluorescence signal from the P_{mnxG} bioreporter started to appear 8 h after the microcolonies entered the stationary phase (Fig. 2a), whereas the signal from the P_{mcoA} bioreporter only appeared 13 h after entry into stationary phase (Fig. 2b). In addition, the maximum fluorescence intensity was reached much earlier in the P_{mnxG} bioreporter than the P_{mcoA} bioreporter (Supplementary Fig. 5a, b), indicating that the timing and rates of expression for both Mn-oxidase genes must be different.

The total reporter fluorescence from the P_{mnxG} microcolonies increased by 29-fold from the start of the activation to its maximum (Supplementary Fig. 5a), but the average fluorescence signal per individual reporting cell in this time interval was approximately constant (Supplementary Fig. 6a, c). Similarly, for the P_{mcoA} bioreporter, the total fluorescence signal increased by 35-fold (Supplementary Fig. 5b), but the average signal per reporting cell varied by less than fivefold (Supplementary Fig. 6b, d). After reaching saturation, the fluorescence signal in both cases

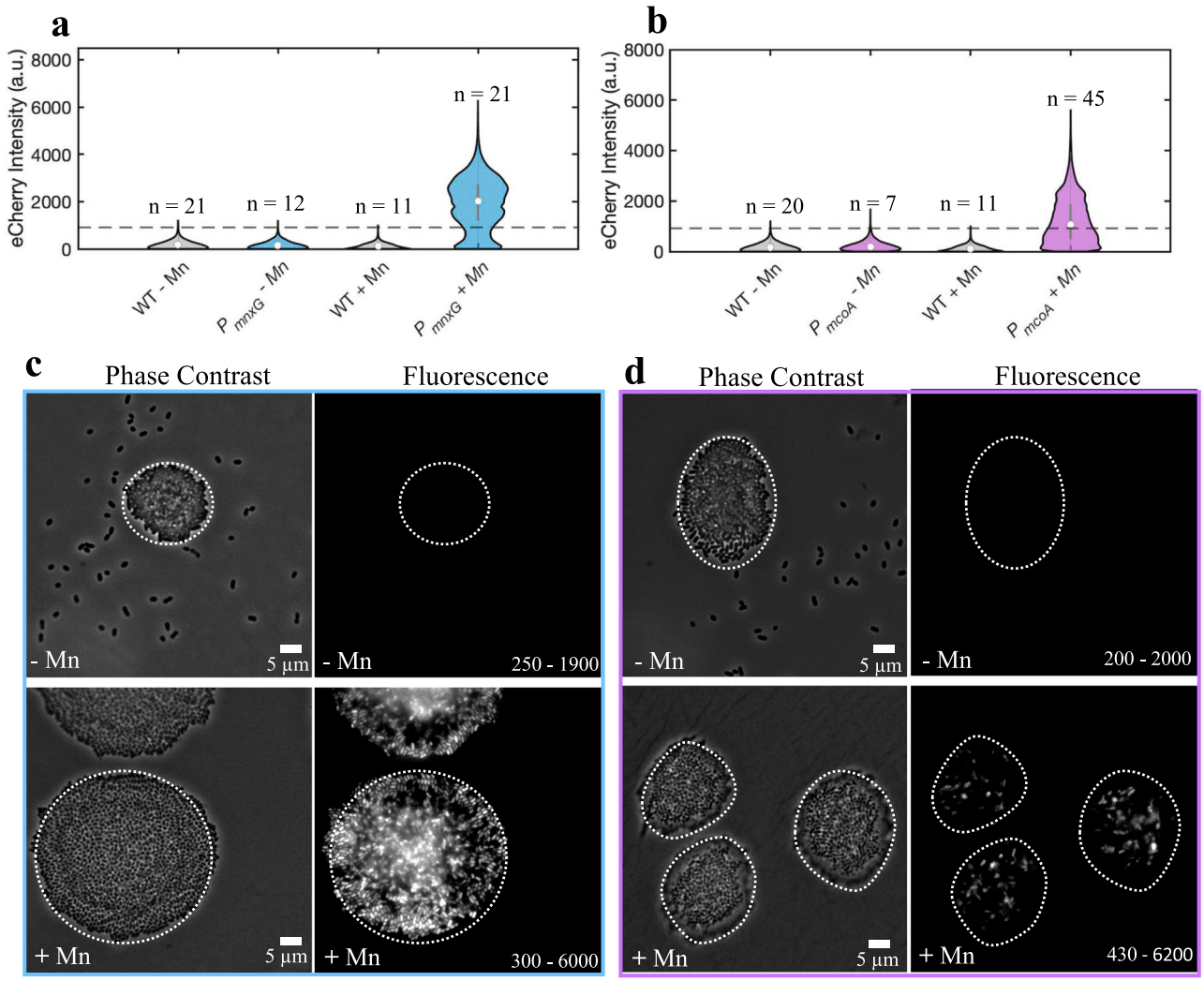

Fig. 1 | Expression of Mn oxidase gene promoters in the presence and absence of Mn(II) in microcolonies of *P. putida* GB-1. a, **b** Violin plot of the fluorescence intensity distribution in microcolonies of wild-type (WT) and bioreporter (P_{mnxG}, **a**; P_{mcoA}, **b**) strains without Mn and with 50 µM Mn(II), where *n* is the number of microcolonies analyzed for each condition. The eCherry fluorescent signal represents the pixel intensity distribution within the boundaries of the microcolonies in the phase contrast images. The fluorescence threshold is set as the 99th quantile of the wild-type distribution, calculated using background-subtracted images. Outliers removed at 6× the *SD* of the respective distributions. **c**, **d** Representative phase contrast and fluorescence images of 48-h-grown *P. putida* GB-1 P_{mnxG} (**c**) and P_{mcoA} (**d**) microcolonies grown in the absence of Mn (top panels) and in the presence of 50 µM Mn(II) (bottom panels). Values on the fluorescence micrographs represent the range of lowest to highest pixel fluorescence signal intensity in the displayed image.

decreased, indicating that promoter activity ceased or was exceeded by photobleaching due to fluorescence excitation (Supplementary Figs. 7 and 8). These results confirm that the increase in total fluorescence from both promoters was driven by an increase in the proportion of activated reporter cells rather than by the increase of fluorescence in individual reporting cells.

Based on the proportion of pixels with fluorescence values above the threshold value, we calculated the maximum proportion of reporting cells within stationary phase microcolonies at 85.1% for the P_{mnxG} bioreporter and 37.6% for the P_{mcoA} bioreporter (Fig. 2a, b). The 95% confidence interval for the maximum active subpopulation was within 9.0% of the mean value for P_{mnxG} ($n = 13$ microcolonies; Figs. 2a), and 15.1% of the mean value for P_{mcoA} ($n = 21$ microcolonies; Fig. 2b). Image analysis of cells grown in liquid-suspended culture revealed similar proportions of cells activating either of the promoters (Fig. 2c, d). However, in liquid cultures at stationary phase conditions, nearly all cells activated the P_{mnxG} promoter (Fig. 2c), whereas only ~60% activated the P_{mcoA} promoter (Fig. 2d). Moreover, the rate of activation of the P_{mcoA} promoter varied with the degree of cell aggregation, such that gene activation was faster within large aggregates (60% of the projected surface area after 20 h) than in planktonic cells (60% of the population activated after 48 h; Fig. 2d). To explore whether the absence of Mn-oxidase gene activation is associated to cell damage, we compared viability of cells with or without fluorescent reporter signal from the same culture. Cells grown in the presence of 50 µM Mn(II) for 48 h were seeded on agarose surfaces to follow cell division in real time. These experiments showed no significant difference in the length of the lag phase or average division time between founder cells with or without previous fluorescent reporter signal, suggesting that reporter expression (and, by analogy, the respective Mn-oxidase gene activation) is not linked to cell viability (Supplementary Fig. 9). Therefore, the observed differences in the timing and proportion of cells showing Mn-oxidase promoter activation among individual cells in stationary phase is not due to differences in cell growth or viability but must reflect an underlying gradient or change in environmental conditions experienced by the cells.

Spatiotemporal patterns in Mn oxidase gene expression within microcolonies

When analyzing the location of reporting cells in microcolonies, we noticed that cells in the center of the microcolonies, corresponding to the location with the highest cell stacking, were among the first to activate P_{mnxG}

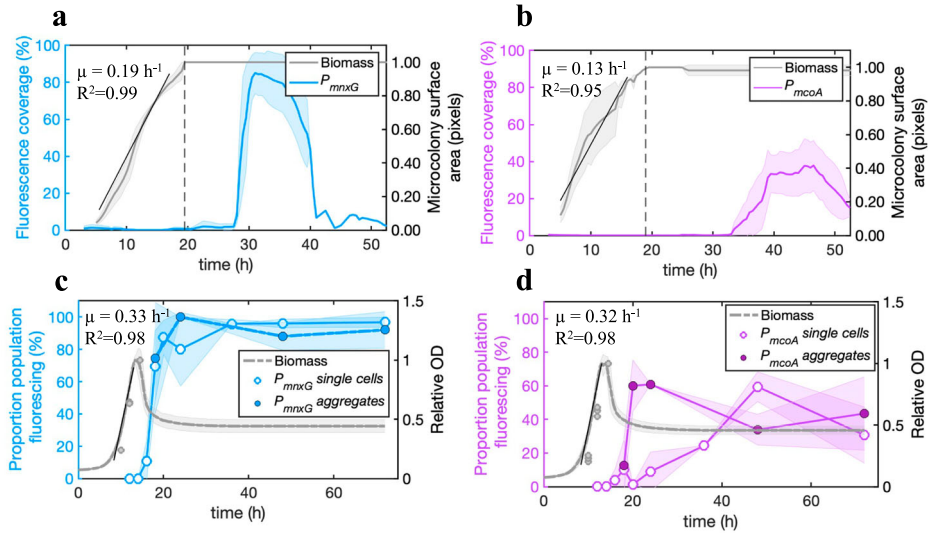

Fig. 2 | Temporal activation of Mn oxidase gene promoters of *P. putida* GB-1 in surface-grown microcolonies and liquid-suspended cultures. a, **b** Surface area of P_{mnxG} (**a**) P_{mcoA} (**b**) fluorescing cells (in blue or magenta) relative to the total microcolony surface area (in gray) at entry into stationary phase as indicated by the dotted lines, expressed as a percent (%). The growth curves, calculated as the increase in microcolony surface area over time, represent the average of 13 replicates for P_{mnxG} and 21 replicates for P_{mcoA}. Shaded areas represent the 95% confidence interval around the mean. Growth rates (μ) are calculated during the exponential phase, as indicated by the black line and its linear regression coefficient (R^2). **c**, **d** Proportion of individual (open symbols) or aggregate cells (closed symbols) fluorescing over time (blue and magenta lines) in liquid-suspended cultures for **c** P_{mnxG} and **d** P_{mcoA}. The shaded areas represent the standard deviation around the mean and are connected for visualization purposes ($n = 3$). Relative OD corresponds to the culture turbidity (as OD_{600}, in gray) normalized by the maximum OD_{600}. Growth curves for liquid-suspended cultures were measured in 5 replicates using a plate reader. The decrease in relative OD after the exponential phase reflects cell aggregation. Separate relative OD_{600} measurements for cultures grown in flasks are shown by the gray symbols.

(Fig. 3a), followed within 1 h by detectable fluorescence in the outer rim of the microcolony (Fig. 3a, c). About 2.5 h later, the bioreporter signal appeared everywhere in the microcolony. The average rate of increase in the P_{mnxG} bioreporter signal was fastest at the microcolony edges (Fig. 3c). These observations suggest that cells in the outermost layer of the microcolony experience optimal conditions for promoter activation. Reporter activation in the P_{mcoA} strain started 5 h later than in the P_{mnxG} strain (Fig. 3b), with a pattern that radiated from the center outwards but never reached the edge of the microcolonies (Fig. 3b, d). These reporter expression patterns were observed consistently among different microcolonies, suggesting that the activation of the Mn oxidase gene promoters results from gradients in chemical cues across the microcolonies.

To verify that the spatiotemporal patterns we observed did not result from the restrictive growth conditions caused by the microscope chambers (i.e., low oxygen availability, Supplementary Fig. 10), we monitored P_{mnxG} and P_{mcoA} activation in open-chamber experiments, where the coverslip was removed to allow for maximum airflow (Supplementary Figs. 10 and 11). We found the same patterns of promoter activation in microcolonies grown in both closed and open chambers (Supplementary Fig. 11). Notably, the proportion of cells activating P_{mcoA} increased with increasing microcolony size (Supplementary Fig. 12), and P_{mcoA} was expressed earlier in the center of cell flocs than in single planktonic cells in liquid culture (Fig. 2d), suggesting more favorable conditions or cues that could activate the P_{mcoA} promoter in dense multicellular aggregates.

Activation of the Mn oxidase gene promoters correlates to the formation of Mn oxide precipitates

To confirm that the bioreporter signal is a faithful representation of the onset of Mn biomineralization, we compared the timing and the extent of reporter fluorescence with the formation of Mn oxide precipitates. Indeed, visible Mn oxide precipitates appeared within an hour of P_{mnxG} activation in both stationary phase microcolonies (Fig. 4a) and liquid-suspended culture (Fig. 4d). While liquid-suspended cultures showed a small amount of Mn removal from solution prior to promoter activation (2.3 ± 0.9 μM Mn(II), Fig. 4d), this loss of Mn from solution resulted from sorption of Mn(II) by the biomass rather than its enzymatic oxidation to Mn(III, IV) (Fig. 4d and Supplementary Fig. 13).

Microcolonies grown under closed chamber conditions typically showed a strong correlation between hotspots of promoter activation and Mn-oxide precipitates (Fig. 4b and Supplementary Fig. 14). These Mn oxide hotspots were concentrated around the edge of the microcolonies (Fig. 4b, c and Supplementary Fig. 14), which coincides with the location of early P_{mnxG} activation (Fig. 3a). Despite the increase in the proportion of P_{mnxG} activation to up to 99.6% ± 0.7% of the microcolonies, Mn oxide precipitates covered only 22.7% ± 2.8% of the microcolony surface after 24 h in stationary phase (Fig. 4a). Since the bioreporter strains have wild-type GB-1 background, microcolonies of the P_{mcoA} bioreporter also showed Mn-oxide precipitates near the microcolony edges (Fig. 4b, c), but these precipitates did not coincide with P_{mcoA} activation. Reporter fluorescence from P_{mcoA} appeared later and in the centre of the microcolonies (Fig. 4a–c) but did not correlate to a further increase in Mn oxide precipitation (Fig. 4a–c). Together, these results demonstrate that MnxG was responsible for the initial formation of Mn-oxides. However, the sparse surface coverage with Mn oxide in other areas of the microcolonies under continued expression of *mnxG* and later expression of *mcoA* suggests that other requirements for mineral precipitation were not fulfilled in the closed chambers.

When experiments were repeated under open chamber conditions in wild-type GB-1, the projected microcolony surface area was fully covered with Mn oxide precipitates (Supplementary Fig. 15a), coinciding with the reporter gene expression observed in the closed chambers (Supplementary Fig. 11). Similar culturing of a GB-1 strain deleted for *mcoA* showed most Mn oxides near the colony edges and less in the colony center, whereas the GB-1 strain deleted for *mnxG* only formed Mn oxides in the colony center (Supplementary Fig. 15a, b). These patterns of Mn oxide formation are similar to the global localization of reporter fluorescence from each Mn-oxidase-specific gene promoter. The presence and sequential activation of two Mn oxidases in GB-1 thus expands the environmental conditions and the time window for Mn biomineralization. Additionally, the reason for the sparser coverage of the microcolonies with Mn oxides in the closed chamber configuration, despite expression of the Mn-oxidase gene promoters, is

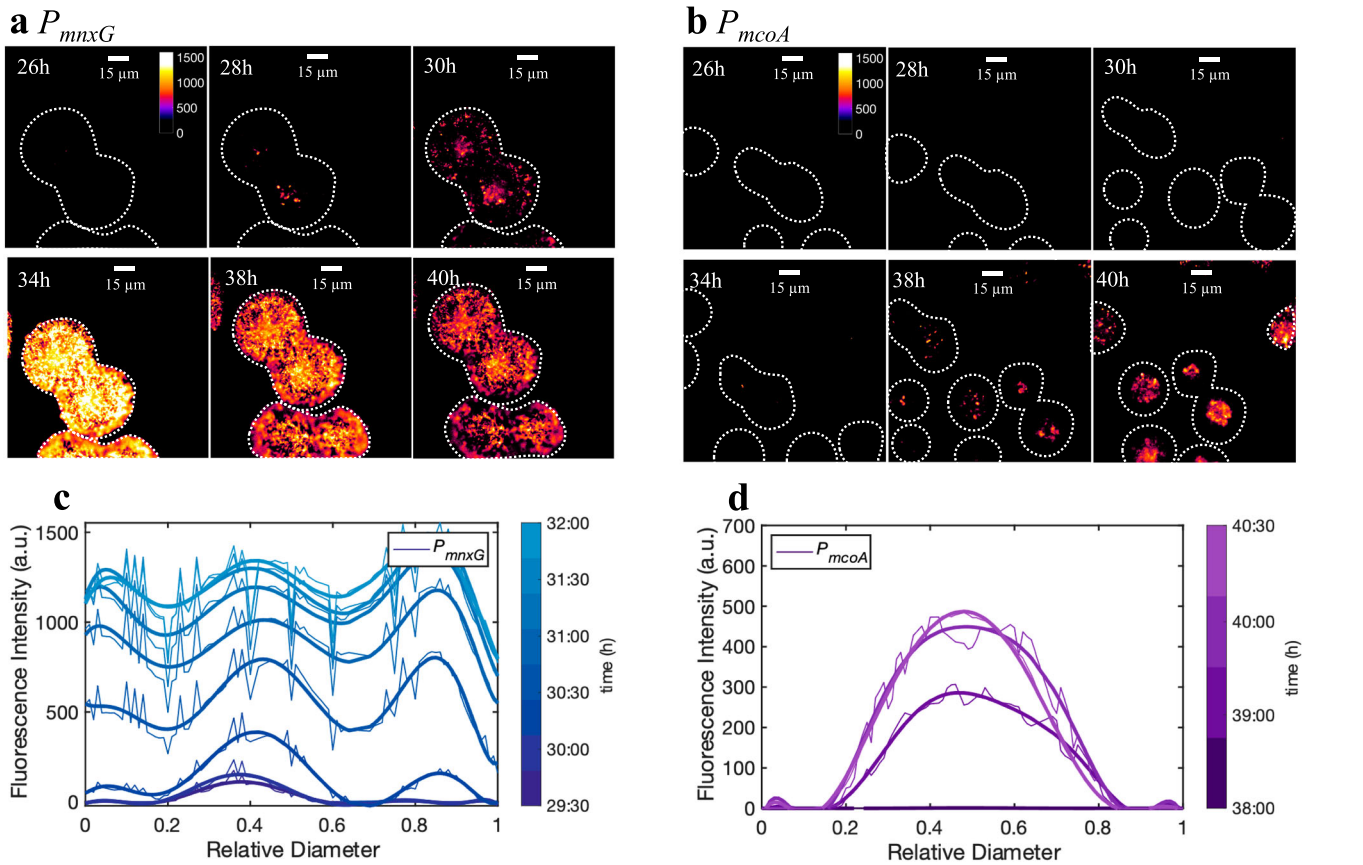

Fig. 3 | Spatiotemporal activation of Mn oxidase gene promoters of *P. putida* GB-1 in surface-grown microcolonies. Microcolonies of P_{mnxG} (**a**) and P_{mcoA} (**b**) bioreporter strains imaged at different times after entry into stationary phase. The fluorescence signal is shown as a heatmap, with values defined as the signal above the threshold. The threshold is the 99th quantile of wild-type GB-1 fluorescence distribution in the reporter wavelengths, calculated using background-subtracted images. The dotted lines show the boundaries of the microcolonies obtained from phase contrast images. Note the later activation of *mcoA* compared to *mnxG*. The decrease in fluorescence intensity for P_{mnxG} after 34 h is due to photobleaching (Supplementary, Fig. 7). **c**, **d** Fluorescence intensity profiles normalized by the microcolony diameter during expression of P_{mnxG} (**c**) and P_{mcoA} (**d**). Profiles represent the average of six replicates for each strain; trends are shown by smoothing using a polynomial. Note the edge appearance of *mnxG* promoter fused fluorescent protein and center appearance of *mcoA*.

likely due to the lower oxygen flux towards the cells[49], which would deprive the enzymes of one of their co-substrates. This oxygen limitation in the closed chambers was removed in the open chamber experiments where the microcolony size increased 10-fold, and Mn oxides covered the entire microcolony surface.

In liquid-suspended culture, we also observed a strong correlation between fluorescent signal appearance and the onset of Mn oxide precipitation for the P_{mnxG} reporter strain (Fig. 4d, e). The formation of Mn oxides around cells and cell aggregates that activated the P_{mnxG} promoter, but had not yet expressed *mcoA* (P_{mcoA} activation appeared ca. 6 h later, Fig. 4e), confirms that MnxG is sufficient for initial Mn oxidation and precipitation (Fig. 4e). By chemically measuring the extent of Mn oxide precipitation, we found that wild-type GB-1 and the *mcoA* deletion strain remove aqueous Mn(II) from solution at the same rate (ca. 0.41 h^{-1}), whereas the *mnxG* deletion strain shows an order of magnitude slower rate (0.04 h^{-1}, Supplementary Fig. 16). Finally, no Mn oxide precipitation was observed in the double knockout strain under the tested conditions (Supplementary Fig. 16). This confirms that MnxG is the main Mn oxidase, followed by McoA, whereas MopA activity is not present.

Discussion

Microbial Mn oxidation was discovered a century ago[50]. This process is performed by a large number of phylogenetically diverse bacteria and fungi[5,15], yet the environmental controls on biomineralization and its physiological function remain elusive[17]. Using fluorescent gene reporters to target the activation of the promoters upstream of *mnxG* and *mcoA* in *P. putida* GB-1, we provide the first temporally and spatially resolved analysis of Mn oxidase promoter activation. We show that reporter activation coincides spatially with Mn oxide precipitation in microcolonies and cellular aggregates, demonstrating that reporter signal can be used to study Mn oxidation at the individual cell level. This approach has provided new insights regarding the regulation of bacterial Mn oxidation, which notably occurs only in non-dividing stationary phase cells and only in the presence of Mn, is confined to subsets of cells within the population, and is different for both Mn oxidase genes.

Previously, Mn biomineralization has been studied based on the extracellular appearance of Mn oxides[5,26,29,33] or by enzyme purification[22], leading to the hypothesis that the presence of multiple Mn oxidases is linked to differences in lifestyle (e.g., biofilm or planktonic cells)[26,31]. Here, we find no evidence for exclusive expression of either *mnxG* or *mcoA* in sessile (microcolonies) or planktonic cells. Instead, *mnxG* and *mcoA* are expressed under both growth conditions. Manganese oxidase gene activation has never been attributed to a specific growth phase, but we can now show beyond doubt, from both surface-grown and liquid-suspended culture experiments, that *mnxG* and *mcoA* are activated during stationary phase conditions and only in the presence of aqueous Mn (Fig. 1 and Supplementary Fig. 5). The requirement of Mn for promoter activation corroborates the finding that additional specific regulatory factors, such as the proposed MnxS1/S2 sensor histidine kinases and MnxR protein[27] are needed to initiate *mnxG* and/or *mcoA* expression[51].

Despite the expression of both *mnxG* and *mcoA* during the stationary phase, their activation was non-uniform in both surface and liquid-grown

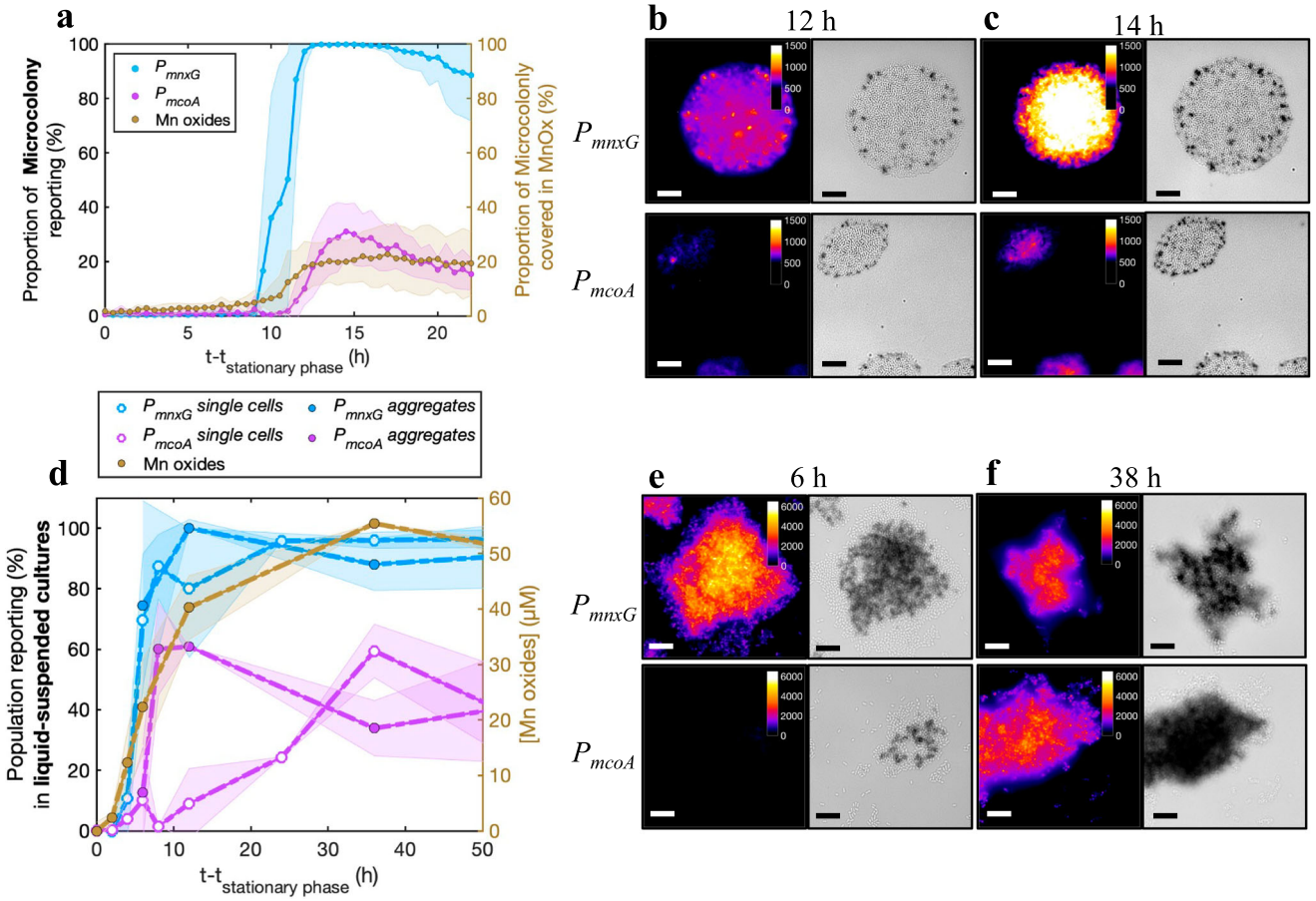

Fig. 4 | Correlation between *mnxG* and *mcoA* promoter activation and Mn oxide formation in *P. putida* GB-1. a Proportion of microcolony area with activated bioreporter fluorescence signal (left axis, above threshold; *mnxG* in blue, and *mcoA* in magenta), and the proportion of microcolony area covered with visible Mn oxide precipitates (right axis, in brown). The time axis is presented as time in (h) after the onset of the stationary phase (reached after 27.5 h on a solid surface). Lines connect the means, and transparent areas represent ± one standard deviation ($n = 20$ colonies analyzed for each reporter). **b**, **c** Representative microscopy images of P_{mnxG} and P_{mcoA} bioreporter microcolonies 12 h (**b**) or 14 h (**c**) in stationary phase for intensity of the eCherry fluorescence (left, according to color scale) or bright field (corresponding Mn oxide precipitates; in gray). Scale bars denote 10 μm. **d** Proportion of activated fluorescent reporter (left axis); *mnxG* in blue and *mcoA* in magenta) as either individual planktonic cells (open circles) or in aggregates (filled circles) in liquid suspended culture, and corresponding fraction of Mn oxides (in μM, right axis) over time after entry into stationary phase (12 h after culture start). The amount of Mn oxide precipitated was calculated by subtraction of the aqueous Mn to the total Mn, as measured by ICP-MS. For visualization purposes, the dotted lines connect sample means with transparent colored areas representing ± one standard deviation ($n = 3$ replicates). **e**, **f** as **b** and **c**, but for aggregates from liquid suspended culture after 6 h (**e**) and 38 h (**f**) into stationary phase. Scale bars represent 10 μm.

cells. First, the proportion of the population expressing either of these genes (by the proxy of the promoter fusion to the fluorescent protein) increased over time for both promoters, with a higher proportion of the population activating *mnxG* than *mcoA*. This bimodal gene activation confers significant phenotypic heterogeneity to individuals within the population of *P. putida* GB-1 cells. Second, the onset of promoter activation relative to entry into the stationary phase differed between the two genes, with *mnxG* being expressed earlier than *mcoA*. Third, the localization of cells expressing either *mnxG* or *mcoA* differed within stationary phase colonies, with *mnxG* expression starting from the edges and moving inward over time, and *mcoA* more confined to colony centers. These observations show that *mnxG* and *mcoA* respond to different chemical gradients forming across the colonies and behave synergistically.

Population-level controls over bacterial gene activation have been attributed to mutation, stress response, intra-population dynamics (e.g., quorum sensing), or variation in chemical conditions (e.g., microenvironments), amongst other factors[47,48,52–54]. This results in increased phenotypic diversity, which enhances the fitness of the population in fluctuating environments[55–57] and enables efficient transitions in and out of stationary phase[58,59]. Although phenotypic heterogeneity at the stationary phase has been observed in other organisms[59–61], studies on bimodal gene expression in *P. putida* are limited. One study shows the heterogeneous production of siderophores among a clonal population associated with improved population fitness by sharing the benefit of producing energy-costly enzymes[56]. In the current study, the high reproducibility between biological replicates, the onset of expression in non-growing cells, and the observed loss of bioreporter signal in exponentially growing cells suggest that the observed bimodality is not the result of a reproducible genetic switch (e.g., phase variation), but is rather a response to environmental cues. Sequential activation of *mnxG* and *mcoA* might result from changes in extracellular conditions, such as pH[62,63] or E_h[64], or secondary metabolites[65,66], which often evolve during bacterial growth in solid and liquid media[67,68]. The delayed activation of *mcoA* relative to *mnxG* and the difference in the timing of *mcoA* activation in cells grown on solid surfaces and liquid-suspended cultures suggests that *mcoA* is more sensitive to environmental conditions encountered later in the stationary phase and prevalent in the colony or aggregate center (Fig. 5). The most common dynamic gradient within microcolonies involves oxygen concentration[49,69–72]. During active colony expansion, oxygen consumption near the edge of the colonies leads to its depletion inside the colony, as observed by Díaz-Pascual et al.[71]. However, once the cells reach the stationary phase, they consume less oxygen and oxygen is replenished towards the colony center within ca. 8 h[71]. The timing

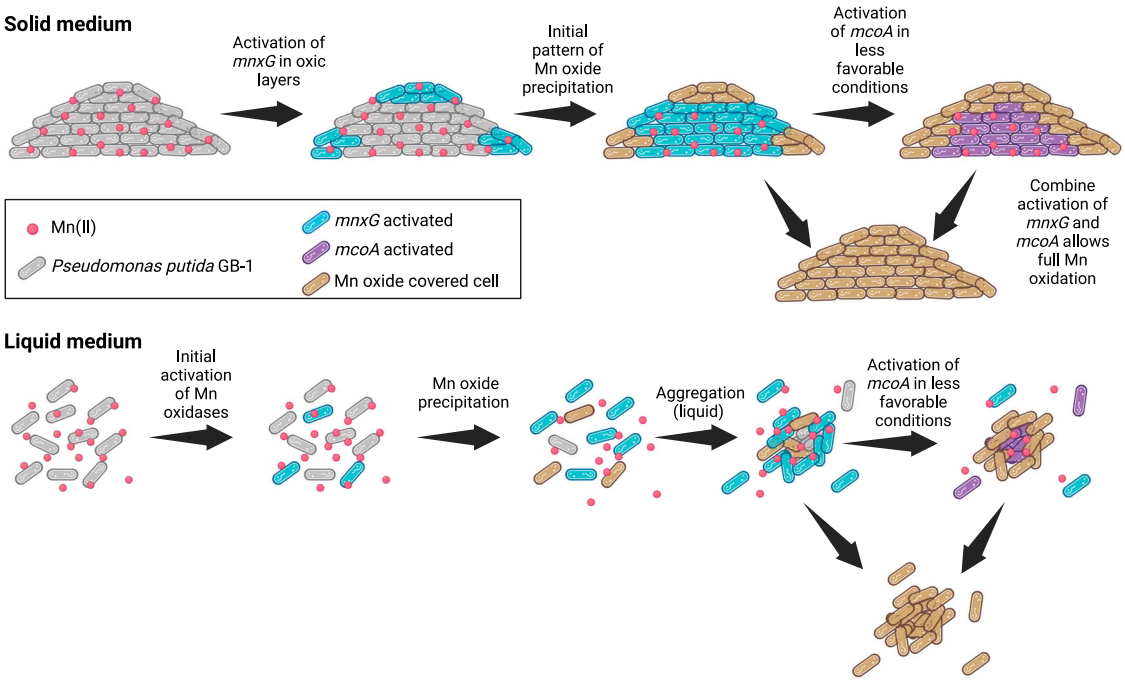

Fig. 5 | Proposed mechanism of promoter activation and Mn oxide biomineralization in *Pseudomonas putida* GB-1. The cells in microcolonies grown to stationary phase in the presence of Mn(II) activate the primary pathway, *mnxG*, under favorable conditions for Mn oxidation (i.e., high O_2 and circumneutral pH). The microenvironment that develops at the center of the microcolony creates less favorable conditions for Mn oxidation, leading to the activation of the second Mn oxidase, *mcoA*. The combined activation of the two enzymes leads to full Mn oxidation and its removal from the solution to the solid phase as Mn oxide. In liquid, the same mechanism is observed, where the aggregate core has less favorable conditions for Mn oxidation, leading to the activation of *mcoA* in the center. The later activation of *mcoA* in single cells likely results from delayed changes in solution chemistry.

of oxygen depletion and renewed diffusion within microcolonies observed by Díaz-Pascual et al. [71] are remarkably similar to the *mnxG* and *mcoA* promoter activation patterns in GB-1 reporter cells. This suggests that oxygen is a co-substrate for Mn oxidase gene activation in the stationary phase, and its flux or local concentration determines expression onset. In this scenario, while the oxygen inflow is replenished to the microcolony edges, *mnxG* is activated, and as oxygen diffusion proceeds to the colony center, *mcoA* becomes activated (Fig. 3 and Supplementary 11). The specific consumption of oxygen associated with MnxG activity and precipitation of Mn oxides may further delay the onset of *mcoA* expression or alternatively trigger *mcoA* activation, if the latter operates at a lower oxygen threshold. The earlier activation of *mcoA* in the center of the cell aggregates compared to single cells (Fig. 2d) confirms that the local conditions created in the center of the aggregates, which are commonly oxygen-limited[73,74], favor activation of *mcoA* (Fig. 5). Future work can now explore how relevant chemical gradients (e.g., Mn, O_2, secondary metabolites, and signaling molecules) and their interactions regulate the heterogeneous expression of the Mn oxidases and subsequent mineral precipitation.

The preferential activation of *mnxG*, as deduced by the earlier timing, broader spatial extent, and occurrence in a higher proportion of the population, concomitant with the precipitation of Mn oxide in all the conditions tested (i.e., closed chambers, open chambers, and liquid medium), demonstrates that MnxG is the dominant oxidase for *P. putida* GB-1. This is supported by experiments with GB-1 strains lacking either *mnxG* or *mcoA*, which show that MnxG alone can oxidize the totality of the Mn(II) supplied (Supplementary Fig. 16), and that McoA is less efficient and remains largely complementary (Figs. 4 and 5). Overall, our results indicate that activation of *mcoA* following activation of *mnxG* can drive Mn oxidation under sub-optimal conditions for MnxG or when its functional capacity is exceeded (Fig. 5).

By carrying multiple Mn oxidases, as regularly found in Mn oxidizers[15], GB-1 can perform Mn oxidation under a wider range of environmental conditions. Bimodal activation of *mnxG* and *mcoA* would lower the cost of producing energetically expensive enzymes in all cells while sharing the benefit of Mn oxide precipitation and/or aqueous Mn(II) removal with the whole population or community. This could be considered a microbial cooperation strategy, as proposed for other metabolic functions, that provides a competitive or ecological advantage[52,57,75,76]. Several hypotheses for the advantage of Mn oxidation for bacteria have been put forward, but none have been firmly demonstrated. For example, Mn oxidation may provide a pathway for metal homeostasis through increased expression of proteins that allow for sequestration of Mn in the solid phase[77], enable the generation of bioavailable carbon substrates from the reaction of Mn oxide and complex organic matter[38], or allow control over extracellular redox conditions to support cell maintenance at stationary phase[78]. Whether this stationary phase process is initiated to rid the extracellular environment of aqueous Mn or to promote the formation of the manganese oxides requires further study. Our discovery that social cooperation within a bacterial population may underlay the formation of biominerals provides a new framework to investigate the function of Mn oxidation and biomineralization not only for individual cells, but for microbial communities and ecosystems.

Methods

Bacterial strains

The strains used in our study are derivatives of *P. putida* GB-1 (Supplementary Table 1). The bioreporters were produced by inserting single copy fusions of the promoter region upstream of either *mnxG* (*2447*) or *mcoA* (*2665*) fused to an *echerry* gene with kanamycin antibiotic resistance on the chromosome of *P. putida* GB-1. *Escherichia coli* DH5alpha was used to propagate plasmid DNA, which then served as a vector for the construction of the reporter gene fusions, while *E. coli* DH5αIpir with kanamycin antibiotic resistance was employed as a host strain for the plasmid construction of the P_{mnxG} and P_{mcoA} bioreporters. Both *E. coli* strains were obtained from the bacterial library of Jan van der Meer (University of Lausanne). All strains were stored at −80 °C in 20% glycerol and 80% LB.

P_{mnxG} and P_{mcoA} bioreporter strains

All enzymes used for DNA digestion or ligation were purchased from New England Biolabs. PCR assays to amplify DNA were performed with primers described in Supplementary Table 2 following the manufacturer's instructions. DNA and PCR products were purified using Nucleospin Gel and PCR Clean-up kits (Macherey-Nagel) according to the manufacturer's instructions.

The promoter region for P_{mnxG} was selected as the 266 base pairs upstream of the gene *mnxG* and the promoter region for P_{mcoA} was selected as the 534 base pairs upstream of the gene *mcoA*, as identified by Geszvain et al.[26] in *Pseudomonas putida* GB-1. These promoter regions were amplified with genomic DNA of *P. putida* GB-1 as a template, using reverse (R) and forward (F) primer pairs PputGB1_2447.F/PputGB1_2447.R and PputGB1_2665L.F/PputGB1_2665.R, respectively (Supplementary Figs. 1 and 2 and Supplementary Table 2). The reporter gene *echerry* (GenBank accession number: AY678264) and its ribosomal binding site (RBS) were amplified on the plasmid DNA pMQ64-echerry[79] using the primer pair eCherry.F/ eCherryTn5.R (Supplementary Table 2). Each promoter region was placed upstream of the *echerry* gene and cloned into SmaI-digested pBAM1[80], using the ClonExpress II one-step cloning kit (Vazyme). This produced plasmids pBAM1(miniTn5::P_{mnxG}-*echerry*), and pBAM1(miniTn5::P_{mcoA}-*echerry*). The resulting plasmids were verified by restriction profiling and DNA sequencing (MycroSynth, Switzerland). Purified plasmid DNA was then introduced into *P. putida* GB-1 by electrotransformation[80–83], which was carried out as described by Dower et al.[84] using 2-mm gap electroporation cuvettes (Cellprojects) and a Bio-Rad GenePulser Xcell apparatus set at 25 µF, 200 Ω, and 2.5 kV for *E. coli* and 2.2 kV for *P. putida*. Clones with a single integrated copy of the mini-transposon reporter construct were selected. Three independent clones of *P. putida* GB-1 with potentially different integration sites of the reporter constructs were purified and stored at −80 °C. Growth rates, fluorescence intensity, and Mn oxide precipitation were tested for each clone and compared to the wild-type (Supplementary Fig. 17 and Supplementary Table 4).

Single and double-knockout mutants

mnxG and *mcoA* single deletion mutants, and a double knockout mutant, were constructed using the two-step chromosomal gene inactivation technique, as described elsewhere[85,86], and using the primers described in Supplementary Table 2. We confirmed the deletion of *mnxG* and *mcoA* by PCR amplification (Supplementary Table 2). The defect of the double knockout mutant on Mn oxidation was confirmed by ICP-MS analysis (Supplementary Fig. 16).

Growth medium and inoculum

Strains were first plated on Luria Broth (LB) containing 1.5% agar containing kanamycin to maintain selective pressure (20 µg ml^{-1} for *E. coli*; 25 µg ml^{-1} for P_{mnxG} and P_{mcoA}; no antibiotic was used for the wild type). Strains were then transferred to liquid LB. *E. coli* was grown overnight in LB medium supplemented with 20 µg/ml kanamycin at 37 °C and shaking at 180 rpm. *P. putida* GB-1 bioreporter strains were grown for 16 h in LB containing 25 µg ml^{-1} of kanamycin at 30 °C in an orbital shaker at 180 rpm. Cells were then centrifuged at 4000 × *g* for 1 min and resuspended in MSTA salt solution (Supplementary Table 3), at room temperature. This step was repeated three times to wash the cell suspension and remove the spent growth medium. The washed cell suspension was then transferred to MSTA, a defined growth medium (Supplementary Table 3) at a starting optical density (OD_{600}) of 0.01. All cell cultures were grown in sterile Erlenmeyer flasks with a 2:5 liquid-to-air ratio, to maintain sufficient oxygenation, at 30°C and orbital shaking at 180 rpm, in the dark.

The MSTA growth medium used to propagate *P. putida* strains contained 0.4 mM $CaCl_2 \cdot 2H_2O$, 0.25 mM $MgSO_4 \cdot H_2O$, 0.25 mM Na_2HPO_4, 0.15 mM KH_2PO_4, 20 µM Fe(III) (added as 1:2 Fe(III):EDTA using 20 µM $FeCl_3 \cdot 6H_2O$ and 40 µM EDTA, pH 6.5), 10 mM HEPES buffer (prepared by adjusting the pH to 7.0 with NaOH), 5 mM $(NH_4)_2SO_4$, 40 nM $CuSO_4 \cdot 5H_2O$, 273 nM $ZnSO_4 \cdot 7H_2O$, 84 nM $CoCl_2 \cdot 6H_2O$, and 53.7 nM $NaMoO_4 \cdot 2H_2O$ and 5 mM L-arginine as the carbon source. The growth medium was complemented with either 0 or 50 µM Mn(II) added as manganese chloride ($MnCl_2$). This growth medium was developed to reduce aggregation of *P. putida* GB-1 cells, which is otherwise commonly observed in complex growth media[26,29,33] (Supplementary Fig. 18).

Bioreporter clone testing

OD and fluorescence intensity were measured with a Varioskan LUX plate reader (Multimode Microplate Reader) using transparent plastic 96 well plates of 350 µL well capacity. A volume of 200 µL of bacteria cultured in MSTA was used to promote oxygenation and mixing. The temperature was maintained at 30 °C and agitation was performed under continuous double orbital shaking at 425 rpm. The OD was measured at 600 nm. The fluorescence was measured in the mCherry channel with excitation at 579 nm and emission at 616 nm. A single measurement of OD and fluorescence consisted of an average of eight measurements in the center of the well with a frequency of 100 ms at 7 mm above the well using a Xenon Flashlight source at high energy. Six replicates were run for each clone. Growth rates were calculated assuming first-order kinetics during the exponential growth phase. The clones were tested against the wild-type to confirm that the Tn5 random insertion did not disturb bacterial growth and/or the ability to precipitate Mn oxide. The five clones were also tested against each other to confirm reporter gene activation. To further confirm that the Tn5 insertion did not affect the Mn oxidation capacity, we systematically compared the Mn(II) oxidation kinetics of the bioreporters against the wild-type and did not find any significant difference (Supplementary Table 4).

Gene expression and Mn oxidation in microcolonies

Microscopy chambers (Helmut Saur Laborbedarf, Germany) were used to follow the growth of single cells over time, the appearance of the fluorescence bioreporter signal, and Mn oxide coverage (Supplementary Fig. 19). Cells were seeded on agarose patches[87] made using MSTA medium and supplemented with 1% agarose, unless otherwise specified. To seed the cells, 3 µl of the washed and diluted cell suspension (OD_{600nm} of 0.01) was deposited onto the agarose patches and sealed into the microscopy chamber. To allow for airflow and oxygenation, we punctured the silicone gaskets on opposite sides, leaving two needles in place throughout the experiment. The microscopy chamber was then mounted on the microscope, which was equipped with a temperature-controlled incubator maintained at 30°C. Epifluorescence microscopy images were acquired every 30 min for 48 h or 54 h. Additional experiments where the microscopy chambers were kept uncovered during bacterial growth and Mn oxidation were conducted in the same way and are referred to as open-chamber experiments. The extent of Mn precipitation within the microcolonies was determined based on color analysis as described below.

Gene expression and Mn oxidation in liquid-suspended cultures

Triplicate cultures for each of *P. putida* GB-1 wild-type strain, P_{mnxG} strain, and P_{mcoA} strain were grown at 30 °C and 180 rpm. Up to eight samples were collected separately for epifluorescence microscopy imaging and ICP-MS measurements between 12 and 72 h. Additional experiments were conducted using the single knockout and double knockout strains, with samples collected at six-time points between 12 and 40 h. For imaging, three microdroplets (4 µl) were deposited on a coated glass slide. To prepare coated slides, 600 µl of a 1% agarose and MSTA salt solution was deposited on the glass slide, which was covered with a second glass slide and allowed to cool before removing the top slide. The extent of Mn precipitation was determined by quantification of Mn in solution and in the solid phase by ICP-MS analysis on filtered or acid-digested aliquots, respectively, as described below.

Viability of reporting cells

To test for the viability of the subpopulations showing P_{mnxG} or P_{mcoA} activation, we first grew the cells in a liquid MSTA medium containing 5 mM L-Arginine and 50 µM $MnCl_2$. After 20 h, we washed the cell

suspension in MSTA salts and inoculated 1% agarose patches containing 5 mM L-Arginine and MSTA salts, in the absence of $MnCl_2$. Cell growth for reporting and non-reporting was then tracked using Dimalis, an image segmentation tool developed for microcolony growth segmentation[88].

Epifluorescence microscopy

P. putida cells were imaged at ×1000 magnification using a Nikon Eclipse Ti2 equipped with a Hamamatsu ORCA-Flash 4.0 camera, a Lumencor Light Engine LIDA 3-color light source, and SOLA III solid-state white light excitation source. Images were acquired in 2048 by 2044 field of view and a pixel resolution of 0.07 μm/pixel. Samples from liquid-suspended cultures were imaged at the edge of the sample to capture planktonic cells and randomly near the center to capture both planktonic and aggregated cells. Cells were imaged in phase contrast (10 ms exposure). eCherry fluorescence was captured by excitation at 562 nm using a SOLA III light engine at 50% intensity and recording emission at 645.5 ± 50 nm (500 ms exposure). Images were stored as 16-bit TIFF files.

Image analysis of microcolonies and aggregates

Phase-contrast images were used to segment microcolonies at the exponential phase using MATLAB R2021b. The contrast was adjusted to the same range for each image by remapping the intensity to fixed values for each image (e.g., time points of a time-lapse). A Gaussian blur was applied to enhance the pixel detection during the binarization. To select the area of interest used for the segmentation and smooth the boundaries of the object, MATLAB's *strel* function was used to dilate and erode in a squared structuring element with a radius of 100 pixels. Each refined image was then used to detect the microcolonies, by first applying the Gaussian blur, adjusting the contrasts (MATLAB, *imadjust*), binarizing (*imbinarize*), filling holes (*imfill*), and smoothing the borders using the "strel" function with diamond structuring element with radius of 15 pixels. Objects of interest were then automatically detected using MATLAB's *regionprops* function. Unwanted objects and agarose crystals were manually removed. The biomass was defined as the pixel area of the segmented microcolony, projected in a 2D plane. To follow biomass growth over time, we selected only microcolonies with a continuous presence in the field of view.

Stationary phase microcolonies and cell aggregates from liquid cultures were also segmented on images using MATLAB R2021b. Images were segmented using the eCherry fluorescence. The background intensity was determined by calculating the median value of the images in which the microcolonies and aggregates covered <50% of the field of view at each time point. The background intensity was then subtracted from the intensity measured at each pixel. Next, the MATLAB built-in function *im2bw* was used to create a binary mask, and to select the pixels corresponding to the biomass. To isolate the aggregates in liquid cultures, we filtered the segmented objects by pixel size and excluded objects with the size of a single bacteria from further processing.

Using the resulting masks and MATLAB's built-in function *regionprops*, we then extracted the fluorescence signal from each aggregate or microcolony (sum of the fluorescence intensity of all pixels divided by the surface area). To discriminate between the fluorescence signal of the bioreporters and autofluorescence from *P. putida* GB-1, we conducted control experiments with the untagged wild-type strain. The bioreporter fluorescence threshold was selected as the 99th quantile of the fluorescence pixel intensity distribution of the wild-type, grown under the same conditions as the bioreporter strains. All signal intensities are reported in arbitrary units (a.u.) (Supplementary Fig. 20).

Image analysis of single cells from liquid cultures

In the case of single (separated) cells on images, we used SuperSegger for segmentation[89], using a trained segmentation constant adapted to the size and shape of *P. putida* at ×1000 magnification[90]. Mean cell fluorescence values (sum of the fluorescent pixels normalized by the cell area) were corrected by subtracting the median background signal outside the segmented cells. Wild-type *P. putida* GB-1 cell images in the eCherry channel were used to identify the cell auto-fluorescence (as the 99th percentile of the wild-type fluorescence distribution) and the threshold above which we considered a 'true' eCherry bioreporter signal appearance. Segmented cells with mean eCherry fluorescence above the threshold were then considered as cells with active promoters (Supplementary Fig. 21). We further report the mean fluorescence bioreporter signal per reporting cell by averaging the individual cell fluorescence across all 'active' cells. The proportion of cells with active P_{mnxG} or P_{mcoA} promoters within a population is then the number of active cells divided by all segmented cells from the corresponding phase-contrast image. Representative results of the segmentation are shown in the false color figures (Supplementary Fig. 21).

Quantification of Mn oxide precipitates on microcolonies by color analysis

Color images were obtained in a separate experiment where more than 20 microcolonies were tracked. The surface area of microcolonies was measured using the same segmentation protocol described above. The proportion of cells within microcolonies that were covered in Mn oxide was quantified using color images obtained from the red, green, and blue color channels, using the 420 nm blue emission filter at 94% brightness, 510 nm green emission filter at 26% brightness, and 590 nm red emission filter at 69% brightness, respectively. All color channels were collected with 16 ms illumination time, and 26 ms of camera exposure, and stored as 16-bit TIFF images. First, the images were inverted to obtain higher pixel intensities for the dark Mn oxide. The contrast was adjusted to the same scale by remapping the intensity to fixed values for each color channel. Images were then blurred, using a Gaussian blur, and the median value of the background of each color channel was subtracted. The brown precipitates of Mn oxide absorbed the transmitted light in the blue channel and did not show any absorption in the red channel (Supplementary Fig. 22). To separate the brown Mn oxide precipitates on the image from any color from the cells, we subtracted the blue channel intensity from the red channel, removed the noise from the resulting image using the *imnlmfilt* MATLAB function, and thresholded the results against the median intensity from images processed in the same manner at the time point prior to visible Mn oxide precipitation. The proportion of the microcolony covered in Mn oxides was then taken as the pixel sum of the identified precipitate 'area' using the regionprops function, divided by the total number of pixels identified as microcolony surface area. The detection limit of the Mn oxide was constrained by the spatial resolution of the microscope (49,000 nm^2). This approach, therefore, can capture agglomerates of Mn precipitates with a diameter of about 220 nm or greater, but cannot identify individual Mn oxide nanoparticles, which can range in diameter from 1 to 10 nm[14].

Quantification of Mn oxide precipitates in liquid cultures by ICP-MS

Aqueous Mn concentrations in the liquid cultures were measured by inductively coupled plasma mass spectrometry (ICP-MS, Agilent-7900). To discriminate between aqueous and solid phase Mn, we measured the aqueous and total Mn concentrations in sample aliquots. For aqueous Mn, we filtered 3 mL of the cell suspension using a 0.22 μm PES filter and acidified to 1% nitric acid prior to analysis. For total Mn, 1 mL of the same cell suspension was digested by adding 30 μL of 65% nitric acid and 100 μl of 0.4 M oxalic acid and then filtered with a 0.22 PES filter to remove the biomass. The ICP-MS was equipped with a quartz spray chamber, a microMist concentric gas nebulizer, nickel sampler, and skimmer cones. ICP-MS analysis was performed in helium (He) mode, using a He flow rate of 4.5 mL min^{-1} with 1.0 L min^{-1} of argon carrier gas. The limit of quantification, which was calculated as 3.3 times the detection limit[91], was 0.04 μg L^{-1} or 0.67 nM for Mn.

Quantification of Mn(II) sorption by the biomass

Sorption experiments were conducted in MSTA containing 50 μM $MnCl_2$, in triplicates. The bioreporter strains were grown for 48 h and aliquot samples were taken during late exponential and stationary phases at 10, 12,

14, 16, 18, and 21 h. Total Mn and aqueous Mn were measured by ICP-MS as described above. The sorbed Mn is reported as the difference between the total Mn and the aqueous Mn. Finally, to confirm that the difference between the total and aqueous Mn originated from the sorbed fraction, we monitored the presence of Mn oxides using the redox dye Leucoberbelin blue[92].

Statistics

All statistical analyses were performed using MATLAB (v. 2024a). Outliers were removed at 6σ for visualization purposes. The proportion of the population reporting included all of the data, calculated as the number of cells with fluorescence values above the 99th quantile of the wild-type fluorescence distribution. All experiments were performed in three to five replicates. Each separate microcolonies were considered as replicates and represented 7–21 replicates for the conditions in the absence of Mn across all experiments. In its presence, the number of replicates represented 11–45 replicates.

Data availability

All data presented in this work are available within the article and the supplementary files. Source data and codes can be found on Dryad data repository at https://datadryad.org/stash/share/LjvLdoQAw6yDTd0_aDyjp3ZyVZpxtPBIawrsgMtP614. Any additional requests can be addressed to the corresponding authors.

Received: 19 September 2024; Accepted: 17 February 2025;
Published online: 24 March 2025

References

1. Gilbert, P. U. P. A. et al. Biomineralization: integrating mechanism and evolutionary history. *Sci. Adv.* **8**, eabl9653 (2022).
2. Cosmidis, J. & Benzerara, K. Why do microbes make minerals? *C. R. Géosci.* **354**, 1–39 (2022).
3. Dreher, C. L. et al. Microbial processes during deposition and diagenesis of banded iron formations. *PalZ* **95**, 593–610 (2021).
4. Ehrlich, H. L., Newman, D. K. & Kappler, A. *Ehrlich's Geomicrobiology*. (2016).
5. Tebo, B. M. et al. Biogenic manganese oxides: properties and mechanisms of formation. *Annu. Rev. Earth Planet. Sci.* **32**, 287–328 (2004).
6. Dong, H. et al. A critical review of mineral–microbe interaction and co-evolution: mechanisms and applications. *Natl Sci. Rev.* **9**, nwac128 (2022).
7. Katiyar, N. K., Goel, G., Hawi, S. & Goel, S. Nature-inspired materials: emerging trends and prospects. *NPG Asia Mater.* **13**, 56 (2021).
8. Malehmir, S. et al. A review of biogenic routes for the manufacture of manganese oxide nanostructures and its anti-cancer, drug delivery, anti-bacterial, and bioimaging potentials. *Inorg. Chem. Commun.* **156**, 111306 (2023).
9. Couradeau, E. et al. An early-branching microbialite cyanobacterium forms intracellular carbonates. *Science* **336**, 459–462 (2012).
10. Yu, H. & Leadbetter, J. R. Bacterial chemolithoautotrophy via manganese oxidation. *Nature* **583**, 453–458 (2020).
11. Spiro, T., Bargar, J., Sposito, G. & Tebo, B. Bacteriogenic manganese oxides. *Acc. Chem. Res.* **43**, 2–9 (2010).
12. Debieux, C. et al. A bacterial process for selenium nanosphere assembly. *Proc. Natl Acad. Sci.* **108**, 13480–13485 (2011).
13. Lefèvre, C. et al. A cultured greigite-producing magnetotactic bacterium in a novel group of sulfate-reducing bacteria. *Science* **334**, 1720–1723 (2011).
14. Romano, C. A. et al. Biogenic manganese oxide nanoparticle formation by a multimeric multicopper oxidase Mnx. *Nat. Commun*. **8**, 746 (2017).
15. Kurdi, M. Z., Olichney, J. & Geszvain, K. A bioinformatic study of the distribution of Mn oxidation proteins in sequenced bacterial genomes. https://doi.org/10.1101/2022.11.10.515945. (2022)
16. Zeiner, C. A. et al. Mechanisms of manganese(II) oxidation by filamentous ascomycete fungi vary with species and time as a function of secretome composition. *Front. Microbiol.* **12**, 610497 (2021).
17. Hansel, C. M. & Learman, D. R. Geomicrobiology of manganese. In: *Ehrlich's geomicrobiology* (eds. Ehrlich, H. L., Newman, D. K. & Kappler, A.) (Taylor & Francis Group, 2016).
18. Hansel, C. M., Zeiner, C. A., Santelli, C. M. & Webb, S. M. Mn(II) oxidation by an ascomycete fungus is linked to superoxide production during asexual reproduction. *Proc. Natl. Acad. Sci.* **109**, 12621–12625 (2012).
19. Remucal, C. K. & Ginder-Vogel, M. A critical review of the reactivity of manganese oxides with organic contaminants. *Environ. Sci. Process. Impacts* **16**, 1247 (2014).
20. Villalobos, M., Lanson, B., Manceau, A., Toner, B. & Sposito, G. Structural model for the biogenic Mn oxide produced by *Pseudomonas putida*. *Am. Mineral.* **91**, 489–502 (2006).
21. Morgan, J. J. Kinetics of reaction between O2 and Mn(II) species in aqueous solutions. *Geochim. Cosmochim. Acta* **69**, 35–48 (2005).
22. Butterfield, C. N., Soldatova, A. V., Lee, S.-W., Spiro, T. G. & Tebo, B. M. Mn(II,III) oxidation and MnO2 mineralization by an expressed bacterial multicopper oxidase. *Proc. Natl. Acad. Sci.* **110**, 11731–11735 (2013).
23. Zhou, M. et al. Surface induced dissociation coupled with high resolution mass spectrometry unveils heterogeneity of a 211 kDa multicopper oxidase protein complex. *J. Am. Soc. Mass Spectrom.* **29**, 723–733 (2018).
24. Andeer, P. F., Learman, D. R., McIlvin, M., Dunn, J. A. & Hansel, C. M. Extracellular haem peroxidases mediate Mn(II) oxidation in a marine *Roseobacter* bacterium via superoxide production: peroxidases mediate superoxide-based Mn oxidation. *Environ. Microbiol.* **17**, 3925–3936 (2015).
25. Learman, D. R. & Hansel, C. M. Comparative proteomics of Mn(II)-oxidizing and non-oxidizing *Roseobacter* clade bacteria reveal an operative manganese transport system but minimal Mn(II)-induced expression of manganese oxidation and antioxidant enzymes. *Environ. Microbiol. Rep.* **6**, 501–509 (2014).
26. Geszvain, K., McCarthy, J. K. & Tebo, B. M. Elimination of manganese(II,III) oxidation in *Pseudomonas putida* GB-1 by a double knockout of two putative multicopper oxidase genes. *Appl. Environ. Microbiol.* **79**, 357–366 (2013).
27. Geszvain, K. & Tebo, B. M. Identification of a two-component regulatory pathway essential for Mn(II) oxidation in *Pseudomonas putida* GB-1. *Appl. Environ. Microbiol.* **76**, 1224–1231 (2009).
28. Geszvain, K., Smesrud, L. & Tebo, B. M. Identification of a third Mn(II) oxidase enzyme in *Pseudomonas putida* GB-1. *Appl. Environ. Microbiol.* **82**, 3774–3782 (2016).
29. Banh, A. et al. Manganese (Mn) oxidation increases intracellular Mn in *Pseudomonas putida* GB-1. *PLoS One* **8**, e77835 (2013).
30. De Vrind, J. P. M., Brouwers, G. J., Corstjens, P. L. A. M., Den Dulk, J. & De Vrind-de Jong, E. W. The cytochrome *c* maturation operon is involved in manganese oxidation in *Pseudomonas putida* GB-1. *Appl. Environ. Microbiol.* **64**, 3556–3562 (1998).
31. Marques Mendonca, R., Fulton, T., Blackwood, C. & Costello, D. Sublethal nickel toxicity shuts off manganese oxidation and pellicle biofilm formation in *Pseudomonas putida* GB-1. *Environ. Microbiol*. 1–16 https://doi.org/10.1111/1462-2920.16529 (2023)
32. Wu, X. et al. Comparative genomics and functional analysis of niche-specific adaptation in *Pseudomonas putida*. *FEMS Microbiol. Rev.* **35**, 299–323 (2011).
33. Parker, D. L. et al. Pyoverdine synthesis by the Mn(II)-oxidizing bacterium *Pseudomonas putida* GB-1. *Front. Microbiol.* **5**, 202 (2014).
34. Toner, B., Fakra, S., Villalobos, M., Warwick, T. & Sposito, G. Spatially resolved characterization of biogenic manganese oxide production within a bacterial biofilm. *Appl. Environ. Microbiol.* **71**, 1300–1310 (2005).

35. Holguera, J. G., Etui, I. D., Jensen, L. H. S. & Peña, J. Contaminant loading and competitive access of Pb, Zn and Mn(III) to vacancy sites in biogenic MnO2. *Chem. Geol.* **502**, 76–87 (2018).
36. Aiken, M. L., Abernathy, M. J., Schaefer, M. V., Lee, I. & Ying, S. C. Inhibition of chromium(III) oxidation through manganese(IV) oxide passivation and iron(II) abiotic reduction. *ACS Earth Space Chem.* **7**, 2327–2338 (2023).
37. Farkas, B. et al. Involvement of bacterial and fungal extracellular products in transformation of manganese-bearing minerals and its environmental impact. *Int. J. Mol. Sci.* **24**, 9215 (2023).
38. Li, H., Santos, F., Butler, K. & Herndon, E. A critical review on the multiple roles of manganese in stabilizing and destabilizing soil organic matter. *Environ. Sci. Technol.* **55**, 12136–12152 (2021).
39. Toner, B. & Sposito, G. Reductive dissolution of biogenic manganese oxides in the presence of a hydrated biofilm. *Geomicrobiol. J.* **22**, 171–180 (2005).
40. Hansel, C. M. & Francis, C. A. Coupled photochemical and enzymatic Mn(II) oxidation pathways of a planktonic *Roseobacter*-like bacterium. *Appl. Environ. Microbiol.* **72**, 3543–3549 (2006).
41. Wright, M., Geszvain, K., Oldham, V., Luther, G. & Tebo, B. Oxidative formation and removal of complexed Mn(III) by *Pseudomonas* species. *Front. Microbiol*. **9**, 560 (2018).
42. Blanco-Romero, E. et al. Genome-wide analysis of the FleQ direct regulon in *Pseudomonas fluorescens* F113 and *Pseudomonas putida* KT2440. *Sci. Rep.* **8**, 13145 (2018).
43. Veening, J.-W., Smits, W. K. & Kuipers, O. P. Bistability, epigenetics, and bet-Hedging in bacteria. *Annu. Rev. Microbiol.* **62**, 193–210 (2008).
44. Jaishankar, J. & Srivastava, P. Molecular basis of stationary phase survival and applications. *Front. Microbiol*. **8**, 2000 (2017).
45. Lange, R., Barth, M. & Hengge-Aronis, R. Complex transcriptional control of the sigma s-dependent stationary-phase-induced and osmotically regulated osmY (csi-5) gene suggests novel roles for Lrp, cyclic AMP (cAMP) receptor protein-cAMP complex, and integration host factor in the stationary-phase response of *Escherichia coli*. *J. Bacteriol.* **175**, 7910–7917 (1993).
46. Fiévet, A., Cascales, E., Valette, O., Dolla, A. & Aubert, C. IHF ss required for the transcriptional regulation of the *Desulfovibrio vulgaris* Hildenborough *orp* operons. *PLoS One* **9**, e86507 (2014).
47. Shingler, V. Signal sensing by σ^{54}-dependent regulators: derepression as a control mechanism. *Mol. Microbiol.* **19**, 409–416 (1996).
48. Dal Co, A., Ackermann, M. & Van Vliet, S. Spatial self-organization of metabolism in microbial systems: a matter of enzymes and chemicals. *Cell Syst.* **14**, 98–108 (2023).
49. Mukherjee, S. & Bassler, B. L. Bacterial quorum sensing in complex and dynamically changing environments. *Nat. Rev. Microbiol.* **17**, 371–382 (2019).
50. Shen, R., Borer, B., Ciccarese, D., Salek, M. M. & Babbin, A. R. Microscale advection governs microbial growth and oxygen consumption in macroporous aggregates. *mSphere* **9**, e00185–24 (2024).
51. Jackson, D. D. A new species of *Crenothrix* (*C. manganifera*). *Trans. Am. Microsc. Soc.* **23**, 31 (1902).
52. Ferré-D'Amaré, A. R. & Winkler, W. C. The roles of metal ions in regulation by riboswitches. *Met. Ions RNA* **9**, 141–173 (2011).
53. Ackermann, M. A functional perspective on phenotypic heterogeneity in microorganisms. *Nat. Rev. Microbiol.* **13**, 497–508 (2015).
54. Dubnau, D. & Losick, R. Bistability in bacteria. *Mol. Microbiol.* **61**, 564–572 (2006).
55. Ochab-Marcinek, A. & Tabaka, M. Bimodal gene expression in noncooperative regulatory systems. *Proc. Natl. Acad. Sci.* **107**, 22096–22101 (2010).
56. Mridha, S. & Kümmerli, R. Coordination of siderophore gene expression among clonal cells of the bacterium Pseudomonas aeruginosa. *Commun. Biol.* **5**, 545 (2022).
57. Smriga, S., Ciccarese, D. & Babbin, A. R. Denitrifying bacteria respond to and shape microscale gradients within particulate matrices. *Commun. Biol.* **4**, 570 (2021).
58. Maria Navarro Llorens, J., Tormo, A. & Martinez-Garcia, E. Stationary phase in gram-negative bacteria. *FEMS Microbiol. Rev.* **34**, 476–495 (2010).
59. Jõers, A. & Tenson, T. Growth resumption from stationary phase reveals memory in Escherichia coli cultures. *Sci. Rep.* **6**, 24055 (2016).
60. Syvertsson, S. et al. Different resource allocation in a bacillus subtilis population displaying bimodal motility. *J. Bacteriol*. **203**, e0003721 (2021).
61. Veening, J. et al. Transient heterogeneity in extracellular protease production by *Bacillus subtilis*. *Mol. Syst. Biol.* **4**, 184 (2008).
62. Ratzke, C. & Gore, J. Modifying and reacting to the environmental pH can drive bacterial interactions. *PLoS Biol.* **16**, e2004248 (2018).
63. Jin, Q. & Kirk, M. F. pH as a primary control in environmental microbiology: 1. Thermodynamic perspective. *Front. Environ. Sci.* **6**, 21 (2018).
64. Hunting, E. R. & Kampfraath, A. A. Contribution of bacteria to redox potential (Eh) measurements in sediments. *Int. J. Environ. Sci. Technol.* **10**, 55–62 (2013).
65. La Rosa, R., Behrends, V., Williams, H. D., Bundy, J. G. & Rojo, F. Influence of the crc regulator on the hierarchical use of carbon sources from a complete medium in *Pseudomonas*. *Environ. Microbiol.* **18**, 807–818 (2016).
66. Molina, L., Rosa, R. L., Nogales, J. & Rojo, F. *Pseudomonas putida* KT2440 metabolism undergoes sequential modifications during exponential growth in a complete medium as compounds are gradually consumed. *Environ. Microbiol.* **21**, 2375–2390 (2019).
67. Fulaz, S. et al. Ratiometric imaging of the in situ pH distribution of biofilms by use of fluorescent mesoporous silica nanosensors. *ACS Appl. Mater. Interfaces* **11**, 32679–32688 (2019).
68. Hwang, G. et al. Simultaneous spatiotemporal mapping of in situ pH and bacterial activity within an intact 3D microcolony structure. *Sci. Rep.* **6**, 32841 (2016).
69. Jeanson, S., Floury, J., Gagnaire, V., Lortal, S. & Thierry, A. Bacterial colonies in solid media and foods: a review on their growth and interactions with the micro-environment. *Front. Microbiol*. **6**, 1284 (2015).
70. Wimpenny, J. W. T. & Coombs, J. P. Penetration of oxygen into bacterial colonies. *Microbiology* **129**, 1239–1242 (1983).
71. Díaz-Pascual, F. et al. Spatial alanine metabolism determines local growth dynamics of *Escherichia coli* colonies. *eLife* **10**, e70794 (2021).
72. Klawonn, I. et al. Distinct nitrogen cycling and steep chemical gradients in *Trichodesmium* colonies. *ISME J.* **14**, 399–412 (2020).
73. Wessel, A. K. et al. Oxygen limitation within a bacterial aggregate. *mBio* **5**, e00992–14 (2014).
74. Lichtenberg, M. et al. The structure–function relationship of *Pseudomonas aeruginosa* in infections and its influence on the microenvironment. *FEMS Microbiol. Rev.* **46**, fuac018 (2022).
75. Kramer, J., Özkaya, Ö. & Kümmerli, R. Bacterial siderophores in community and host interactions. *Nat. Rev. Microbiol.* **18**, 152–163 (2019).
76. Özkaya, Ö., Xavier, K. B., Dionisio, F. & Balbontín, R. Maintenance of microbial cooperation mediated by public goods in single- and multiple-trait scenarios. *J. Bacteriol*. **199**, e00297-17 (2017).
77. Habjanič, J., Mathew, A., Eberl, L. & Freisinger, E. Deciphering the enigmatic function of *Pseudomonas* Metallothioneins. *Front. Microbiol.* **11**, 1709 (2020).
78. Husson, O. Redox potential (Eh) and pH as drivers of soil/plant/microorganism systems: a transdisciplinary overview pointing to integrative opportunities for agronomy. *Plant Soil* **362**, 389–417 (2013).
79. Shaner, N. C. et al. Improved monomeric red, orange and yellow fluorescent proteins derived from *Discosoma* sp. red fluorescent protein. *Nat. Biotechnol.* **22**, 1567–1572 (2004).

80. Martinez-Garcia, E., Calles, B., Arevalo-Rodriguez, M. & de Lorenzo, V. pBAM1: an all-synthetic genetic tool for analysis and construction of complex bacterial phenotypes. *BMC Microbiol.* **11**, 38 (2011).
81. Choi, K.-H. et al. A Tn7-based broad-range bacterial cloning and expression system. *Nat. Methods* **2**, 443–448 (2005).
82. Koch, B., Jensen, L. E. & Nybroe, O. A panel of Tn7-based vectors for insertion of the *gfp* marker gene or for delivery of cloned DNA into Gram-negative bacteria at a neutral chromosomal site. *J. Microbiol. Methods* **45**, 187–195 (2001).
83. Bao, Y., Lies, D. P., Fu, H. & Roberts, G. P. An improved Tn7-based system for the single-copy insertion of cloned genes into chromosomes of Gram-negative bacteria. *Gene* **109**, 167–168 (1991).
84. Dower, W. J., Miller, J. F. & Ragsdale, C. W. High efficiency transformation of *E. coli* by high voltage electroporation. *Nucleic Acids Res.* **16**, 6127–6145 (1988).
85. Martínez-García, E. & De Lorenzo, V. Engineering multiple genomic deletions in Gram-negative bacteria: analysis of the multi-resistant antibiotic profile of *Pseudomonas putida* KT2440: tools for editing gram-negative genomes. *Environ. Microbiol.* **13**, 2702–2716 (2011).
86. Miyazaki, R. et al. Cellular variability of RpoS expression underlies subpopulation activation of an integrative and conjugative element. *PLoS Genet.* **8**, e1002818 (2012).
87. Reinhard, F., Miyazaki, R., Pradervand, N. & van der Meer, J. R. Cell differentiation to "mating bodies" induced by an integrating and conjugative element in free-living bacteria. *Curr. Biol.* **23**, 255–259 (2013).
88. Helena-todd. Dimalis: a new way of analysing your timelapse images fast and efficiently. https://www.biorxiv.org/content/10.1101/2024.04.23.590675v1.full (2022).
89. Stylianidou, S., Brennan, C., Nissen, S. B., Kuwada, N. J. & Wiggins, P. A. SuperSegger: robust image segmentation, analysis and lineage tracking of bacterial cells. *Mol. Microbiol.* **102**, 690–700 (2016).
90. Delavat, F., Mitri, S., Pelet, S. & Van Der Meer, J. R. Highly variable individual donor cell fates characterize robust horizontal gene transfer of an integrative and conjugative element. *Proc. Natl. Acad. Sci*. **113**, E3375-83 (2016).
91. Hein, C., Sander, J. M. & Kautenburger, R. New approach of a transient ICP-MS measurement method for samples with high salinity. *Talanta* **164**, 477–482 (2017).
92. Cavazos, A. R. & Glass, J. B. Simul-staining manganese oxides and microbial cells. *Limnol. Oceanogr. Methods* **18**, 362–373 (2020).

Acknowledgements

We thank Dr. Vladimir Sentchilo for his help in the development of the bioreporters, Dr. Kyounglim Kang for her assistance with ICP-MS, Tania Miguel Trabajo for providing training in the use of the sealed microscope chambers, and Konane Gurfield for her help with image collection. We are also grateful to Eleanor Fadely, Dr. Kyounglim Kang, and Dr. Sharon Bone for their helpful discussions. This work was supported by the Swiss National Science Foundation (200021_188546) and the U.S. National Science Foundation (1449501 and 2322428). The funder played no role in the study design, data collection, analysis, and interpretation of data, or the writing of this manuscript.

Author contributions

G.G., J.R.M., and J.P. designed the study. N.C. designed and constructed the bioreporters. G.G. did the experimental work and collected data. G.G. wrote the codes for image analysis and data processing. G.G., N.C., J.R.M., and J.P. wrote the manuscript.

Competing interests

The authors declare no competing interests.

Additional information

Supplementary information The online version contains supplementary material available at https://doi.org/10.1038/s41522-025-00670-5.

Correspondence and requests for materials should be addressed to Jasquelin Peña.